Directional band gap phononic structures for attenuating crosstalk in clamp-on ultrasonic flowmeters

Valappil, Sabiju Valiya; Aragón, Alejandro M.; Goosen, Johannes F.L.

Directional band gap phononic structures for attenuating crosstalk in clamp-on ultrasonic flowmeters

Sabiju Valiya Valappil, Alejandro M. Aragón, Johannes F.L. Goosen *

Faculty of Mechanical Engineering, Delft University of Technology, Mekelweg 2, Delft, 2628 CD, The Netherlands

ARTICLE INFO

ABSTRACT

Clamp-on ultrasonic flowmeters suffer from crosstalk—i.e., measurement errors due to the interference of signals generated in solid regions and solid–fluid interfaces with the required signal from the fluid. Although several approaches have been proposed to alleviate crosstalk, they only work in specific ranges of flow rates and pipe diameters, and some also introduce additional issues. We propose a novel clamp-on system design where the transmitting and receiving wedges are embedded with directional noise filtering mechanisms based on phononic crystals (PnCs) possessing directional band gaps (DBGs). PnCs are artificial materials consisting of periodic structures arrayed in a matrix medium exhibiting band gaps – i.e., frequency ranges where waves are attenuated – due to Bragg scattering. DBGs enable PnCs to propagate waves in specific directions while suppressing them in other directions. By guiding the input signal through the transmitting wedge to the wall, we minimize the generation of noise signals due to secondary reflections within the wedge. Similarly, by using the directionality of the DBG PnC in the receiver, we limit the effects of noise signals (that arrive in different directions) in the receiver. We numerically verify the DBG PnC embedded wedges' performance by comparing wave propagation aspects of the PnC embedded clamp-on system with a standard clamp-on device. To that end, we develop accurate wave propagation models based on the Discontinuous Galerkin finite element method. By incorporating DBG PnCs into the wedges, we obtain about 20 dB increase in the signal-to-noise ratio compared to the clamp-on system with standard wedges.

1. Introduction

Flow metering is a quintessential process in many industries to ensure quality and smooth operation, and its market size is predicted to reach $12.99 billion by 2028 [1]. Flow meters are used in various applications, such as pharmaceutical [2], oil and natural gas [3], automotive [4], aerospace [5], and medical diagnostics [6], among others. They are classified as variable area type, pressure-based, optical, magnetic type, Coriolis, and ultrasonic devices [7]. Ultrasonic flowmeters (UFs) can be further divided into in-line and clamp-on devices, which provide accurate measurements since they can be used without disrupting the flow. Additionally, they are very versatile as we can use them with a wide range of pipe sizes and various types of fluids. Despite all these advantages, in-line UFs are difficult to install since, for an accurate measurement, it is necessary to know the arrangement of transducers, for which the manufacturer needs to know *a priori* the size of the pipeline and the properties of the flowing fluid. These parameters are
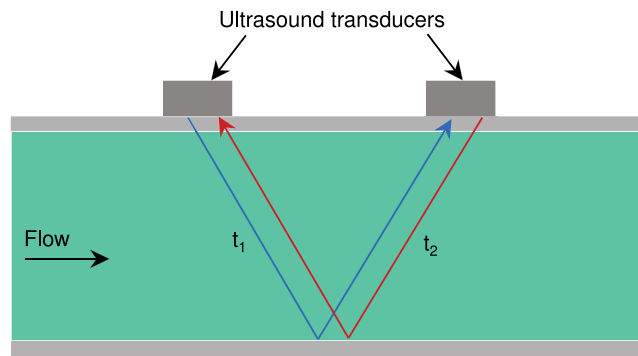
Fig. 1. Schematic representation of the operation of a clamp-on UF, where t_1 and t_2, respectively, represent the upstream (towards the flow direction) and downstream (against the flow direction) travel times whose difference is proportional to the flow rate. (For interpretation of the references to color in this figure legend, the reader is referred to the web version of this article.)

not always known. Moreover, the flow needs to be temporally interrupted to install these flowmeters, which may lead to pressure drops, fouling, and leakage [8].

Clamp-on flowmeters do not have these limitations since they are portable devices that can be installed to a pipe wall effortlessly without disrupting the flow and without introducing additional pipe sections. Moreover, they offer measurement in wide flow ranges and are less expensive than their in-line counterparts [9] . Since the device is not directly in contact with the measuring fluid, the maintenance cost is practically negligible [10]. Clamp-on UFs operate based on the transit-time principle as shown in Fig. 1. In a clamp-on UF, the ultrasound signal generated by a piezoelectric transducer (piezo) is transmitted to the pipe wall, which then enters into the fluid in contact. After traveling through the fluid, this wave is transmitted back to the pipe wall and is received by the receiving piezo (blue line from the figure). The exact process is repeated in the opposite direction (red line in the figure), and the difference in the travel time between these two signals provides us with information about the flow rate of the fluid. However, the input signal also excites other types of parasitic waves, such as pressure (P) waves and Lamb waves in the pipe wall [11], which interact with the required signal through the fluid, resulting in crosstalk between these signals. Due to crosstalk, the flowmeter experiences measurement issues such as a reduction in accuracy or the loss of the necessary signal.

Several solutions have been proposed to reduce these interactions in the clamp-on UFs, thereby improving the measurement accuracy. Sanderson and Yueng proposed a design where an absorbing layer is placed around the pipe wall between the transducers that attenuates the interfering Lamb waves [8]. However, in many cases, the pipe may be covered by materials for heat protection, thus limiting access to the pipe wall and making this approach less viable. Tezuka et al. modified the wedge angle that couples the transducer to the pipe wall to minimize the generation of Lamb waves [12]. Nevertheless, modifications in the wedge angle would require manual adjustment of transducers, thereby making the process operator-dependent. Wang et al. used metallic wedges made of stainless steel instead of polymer (which are commonly used) and excited the wedges' shear modes, which in turn induce shear waves in the pipe wall, thereby reducing the P wave generation [13]. However, the additional interfaces (to produce a shear wave in the wedge) introduce multiple reflections, which inherently induce various waves in the pipe wall that could interfere with the required signal, further reducing measurement accuracy.

Array-based sensors can circumvent the usage of wedges, thereby avoiding manual calibration and reducing multiple wave interactions, thus improving the measurement accuracy [10]. They consist of an array of piezoelectric sensors that are wrapped around the pipe, and the flow rate is measured using array processing techniques [14]. These sensors possess high accuracy and repeatability. Moreover, since no coupling compound (generally applied between wedges and the pipe wall) is needed, no maintenance is required. Nevertheless, the flow rate should be greater than 0.9 m/s, they have long start-up time, and they put restrictions on the pipe diameter (which should be greater than 5 cm) [10]. Another type of transducer array, known as a matrix transducer array, has been used to minimize the Lamb waves in the pipe wall while maintaining the required beam shape in the fluid with a flat wave front [15]. Unlike the previously mentioned sensor arrays, the matrix transducer array uses spatially arranged small-sized piezo elements with a much smaller spatial footprint than the array-based sensors (sub-millimeter) separated by air [16]. By using electronic beam steering techniques, matrix arrays can adjust the angle and the shape of the wavefront [17], enabling them to produce multiple beams in different directions, thereby improving the measurement accuracy. However, the steering and focusing are only possible in the near field, and a larger aperture is required otherwise. Another significant issue is the generation of electric crosstalk caused by the deficiency of electromagnetic shielding, the capacitive effects between the elements, or close electric connections [18]. This crosstalk can deteriorate the directivity of the ultrasonic beam and accidental excitation of a piezo element by the adjacent element, reducing the capacity to control the beam.

A solution to reduce the interference of waves from the pipe wall and the fluid, without introducing additional crosstalk, could be attained by using phononic crystals (PnCs) [19,20]. PnCs are artificial periodic structures possessing unusual dynamic characteristics, such as band gaps (BGs), which are frequency ranges where the propagation of mechanical waves is attenuated. These BGs are generated due to destructive interference of waves when the unit cell dimensions are comparable to the incoming wavelength, similarly to Bragg scattering of electromagnetic waves [21]. PnCs are employed in various applications such as vibration

Table 1

Material properties of various parts of the clamp-on system. Polysulfone is used in the wedge region, whereas the pipe wall is made of stainless steel, and the measuring fluid is water.

Material	Density (kg/m^3)	Pressure wave speed (m/s)	Shear wave speed (m/s)
Polysulfone	1350	1958.84	1183.38
Stainless steel	7800	4935.5	3102.9
Water	998.2	1481.4	–

isolation [22], frequency steering [23], acoustic cloaking [24], energy harvesting [25], and super/hyper lens [26,27]. PnCs have also been designed and optimized to possess directional BGs (DBGs) thereby attaining specific wave propagation behavior such as unidirectional transmission [28,29]. We have previously used PnC structures in an in-line UF to improve its measurement accuracy by minimizing the crosstalk levels [30,31]. They have also been applied in non-invasive ultrasonic transducers to enhance the sensitivity of liquid sensors [32,33]. Other similar applications of PnCs in a clamp-on setting include enhancing sensing capabilities of gasoline property detection systems [34,35], improving transducer's accuracy during non-destructive evaluation [36,37], aiding in structural health monitoring [38–40], detecting and sensing nonlinear elastic sources [41,42] and guided waves [43]. To the best of our knowledge, PnCs have yet to be used in a clamp-on UF to improve measurement accuracy by minimizing the interference of waves between the pipe and the fluid.

In this study, we investigate the feasibility of using PnCs with directional wave propagation behavior because of the presence of DBGs to improve the measurement accuracy of clamp-on UFs. We first build accurate wave propagation models of the complete clamp-on system based on the discontinuous Galerkin method (DGM) [44]. Further, we develop standard finite element models of PnC structures, which possess directional BGs that enable wave propagation only through specific directions. Using the band structure and transmissibility analyses, we evaluate the performance of the PnC structures. The PnC waveguide is incorporated into the wedge section of the clamp-on system to steer the incoming waves to desired directions while minimizing the transmission of waves in other directions, thereby reducing the undesirable wave generation in the pipe wall. The performance of the PnC-incorporated transducer is compared against a standard transducer via transient analysis using DGM models.

2. Clamp-on ultrasonic flowmeter: operation and noise generation

We begin by defining the clamp-on UF geometry and material parameters. The clamp-on system consists of a fluid-filled pipe, an acoustic transmitter, and a receiver, as shown in the schematic Fig. 2(a). The pipe is made of stainless steel, while the fluid used is water. Additionally, the wedges used in the clamp-on flowmeter are generally constructed from polysulfone (PSU), a high-performance thermoplastic with superior corrosion resistance [45]. The relevant properties of these materials are listed in Table 1. These properties are used to calculate the signal path through the clamp-on system.

2.1. Clamp-on ultrasonic flowmeter characteristics

Fig. 2(b) shows the 2D sectional view (through the center of the pipe along its length) of the clamp-on UF, where signal and noise paths and various angles are marked. Commonly used clamp-on UF has a target central frequency of 1 MHz, which we select for the input pulse. Schematics of an input signal and the resulting output pulse that includes both the signal via the fluid and the noise are also illustrated in the figure. During the operation of the clamp-on UF, the input electric signal is converted to an ultrasound pulse by piezoceramic elements (not shown in the figure) that are attached to wedges. This ultrasound signal generates a P wave in the transmitting wedge, which then travels to the wedge-pipe wall interface, where part of it reflects back to the wedge while another part transmits to the pipe wall. This transmitted signal then travels through the pipe wall–fluid interface and, similarly to the previous case, experiences reflection and refraction; thus, part of it enters the fluid domain. After traveling through the fluid, this signal enters the receiving wedge via the pipe wall, where the attached piezoceramic elements convert the acoustic wave to an electric signal to provide the travel time that aids in determining the flow rate. Noteworthy, the signal path is affected by the orientation of the wedges, operational frequency, and pipe diameter. Thus, the fluid signal can travel in an inclined line, a V-shape (used here), or a W-shape, depending on which the number of fluid-solid interfaces can vary.

The angles that determine the signal path, ϕ_1, ϕ_2, and ϕ_3, respectively, are the angle of incidence of the ultrasonic signal from the piezo, the refraction angle at the wedge-pipe wall interface, and the refraction angle to the fluid. These angles are calculated using ray acoustics since, at high frequencies, such as in the current situation, ray approximation can provide accurate predictions of refraction angles using Snell's law [46]:

$$\frac{\sin \phi_1}{c_1} = \frac{\sin \phi_2}{c_2},$$

(1)

where c_1 and c_2, respectively, are the sound speeds of medium 1 (where the incoming wave comes from) and medium 2 (where the wave travels to). ϕ_1 is the incident angle in medium 1, while ϕ_2 is the refraction angle in medium 2. ϕ_1 is equivalent to the angle of the wedge, which is 30° (market standard for clamp-on UFs). From the material properties in Table 1 and using Eq. (1), we get $\phi_2 = 52.4°$, and $\phi_3 = 22.2°$, respectively. Since the wedge-pipe wall is a solid–solid interface, an incoming P wave would refract a P wave and a shear (S) wave at this interface. This results in multiple signals in the measuring fluid and pipe wall, leading to difficulties
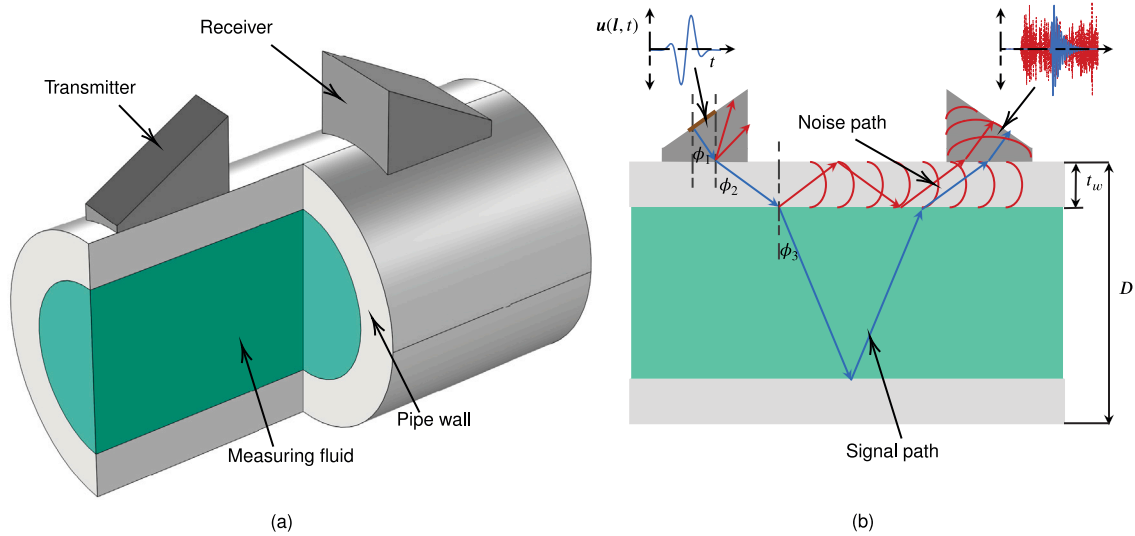
Fig. 2. Schematic of the clamp-on system. (a) 3D view where transmitting and receiving wedges, the pipe wall, and the internal fluid are marked with arrows. (b) 2D view of the center plane with different signal and noise paths, refraction angles, pipe diameter D, and wall thickness t_w. Blue arrows represent the required signal path, whereas red arrows and curves constitute noise paths. l represents the location on the wedge where the input displacement u is applied (marked in (b)). Input displacement's time response $u(l, t)$ is shown above the left wedge, while a schematic of the output displacement (signal and noise) is displayed above the right wedge. (For interpretation of the references to color in this figure legend, the reader is referred to the web version of this article.)

in the measurement process. To avoid this complication, the wedge is designed such that ϕ_1 is always larger than the first critical angle so that P waves experience total internal reflection; therefore, only S waves are present in the pipe wall. Additionally, to ensure S waves are always present, ϕ_1 is always kept lower than the second critical angle (critical angle for S waves). The dimensions of the wedge (36 mm base and 22.5 mm height), and the pipe (diameter $D = 80$ mm and wall thickness $t = 4$ mm) are selected from a commercially used clamp-on UF (Krohne OPTISONIC 6300). These dimensions and the aforementioned angles can provide the signal path length, which determines the exact location of the receiving wedge for precise detection of the measuring signal. We call signals constituting this wave path the primary signals (marked using blue arrows in Fig. 2(b)); we discuss below various other signals and their paths. Although we can obtain the primary signal path accurately by using ray tracing (via ray acoustics), the noise path is more complicated due to the presence of different types of waves (P, S, and Rayleigh), their interactions, and the presence of multiple wavefronts (planar and cylindrical) and boundaries. To investigate the influence of these aspects in the measurement process, we study wave propagation through different domains of the clamp-on system.

2.2. Wave propagation through the clamp-on flow meter

Wave propagation in the clamp-on device shown in Fig. 2 is governed by elastic and acoustic wave equations. Since at 1 MHz constructing high-fidelity 3D wave propagation models is challenging because of the enormous computational cost associated, we analyze the entire system in 2D (as shown in Fig. 2(b)). Thus, we use the 2D elastic wave equation to describe the wave propagation through the wedges and the pipe wall:

$$\rho_s \ddot{u} = (\lambda_s + 2\mu_s)\Delta u - \mu_s \nabla \times \nabla \times u, \tag{2}$$

where, $u(x, t)$ and $\ddot{u}(x, t)$ are, respectively, the planar (x–y plane) displacement and acceleration at the spatial coordinate x and time t. ρ_s represents the density, λ_s, and μ_s are the Lamé coefficients of the solid material, whereas Δ and $\nabla \times$, respectively, represent the Laplacian and curl vector operators. The stresses and strains within the solid domains are related by the following constitutive equation, $\sigma = C : \epsilon$, where σ and ϵ are, respectively, the Cauchy stress tensor, and the strain tensor (both 2nd order), while C is the 4th order elasticity tensor. Similarly, the wave propagation through the fluid domain can be represented using a 2D acoustic wave equation. As two wave fields (pressure and velocity) are present in the fluid domain, we can use either to represent wave propagation:

$$\Delta p = \rho_f \beta \ddot{p}, \qquad \Delta v = \rho_f \beta \ddot{v}, \tag{3}$$

where $p(x, t)$ and $v(x, t)$, respectively, represent the pressure and velocity fields, while β is the compressibility of the fluid and ρ_f its density. We use interface conditions to connect different domains. The wedge-pipe wall interface is defined using a solid–solid contact pair, which dictates that the displacements and tractions across the interface should be the same for both regions:

$$\boldsymbol{u}_1 = \boldsymbol{u}_2, \qquad \boldsymbol{\sigma}_1 \cdot \boldsymbol{n}_1 = \boldsymbol{\sigma}_2 \cdot \boldsymbol{n}_2, \tag{4}$$

where 1 and 2, respectively, are the solid region 1 and region 2 in contact, and $\boldsymbol{n}$ is the unit outward normal vector along the interface. Coupling the pipe-fluid interface is more complicated since the field variables are different in both domains. We couple elastic and acoustic wave equations using a kinematic interface condition that ensures the continuity of normal components of the velocity along the interface as follows:

$$\boldsymbol{n} \cdot \nabla p = -\rho_s \boldsymbol{n} \cdot \ddot{\boldsymbol{u}}, \tag{5}$$

where ∇ is the gradient operator. Additionally, we need a dynamic interface condition to ensure the continuity of the traction along the interface:

$$-p\boldsymbol{n} = \mu_s \frac{\partial \boldsymbol{u}}{\partial \boldsymbol{n}} + (\lambda_s + \mu_s)(\nabla \cdot \boldsymbol{u})\boldsymbol{n}. \tag{6}$$

The details of these interface conditions can be found in [47]. We still require boundary conditions (BCs) for the wave propagation analysis. We supply a Dirichlet BC (prescribed displacement) along the boundary of the transmitting wedge where the piezo is attached (marked using a brown-thick solid line in the left wedge of Fig. 2(b)) while keeping the remaining outer boundaries traction free (homogeneous Neumann BC). The former BC takes the form

$$\boldsymbol{u}(\boldsymbol{l}, t) = \bar{\boldsymbol{u}}g(t), \quad \text{applied at} \quad \underline{x = \underline{l}}, \tag{7}$$

where $\bar{\boldsymbol{u}}$ is the constant displacement amplitude that is multiplied by the function $g(t)$, which determines the time response. We use a sinusoidal pulse to represent $g(t)$ (the function $\boldsymbol{u}(\boldsymbol{l}, t)$ is shown in Fig. 2(b) above the left wedge). The input signal in the frequency domain is a Gaussian pulse having a central frequency of 1 MHz with a -6 dB bandwidth of 1 MHz (the explanation of the frequency-domain pulse is provided in Section 0.1 of the supplementary material). By using the wave Eqs. (2) and (3), interface conditions (4), (5), and (6), and the boundary condition (7), we have everything to set up the numerical analyses required to obtain information about various traveling waves in the clamp-on flowmeter.

2.2.1. Wave propagation analysis using DGM

We select DGM to analyze the wave propagation since this approach is suitable for arbitrary time-dependent sources and fields. The method is adequate for modeling elastic and acoustic wave propagation over large distances relative to the wavelength, such as in the present case, where the signal path length is 220 mm, while the smallest wavelength is 0.8 mm (signal wavelength of 1.5 MHz (highest signal frequency) in the PSU wedge.) The Comsol implementation uses a time-explicit solver and is memory efficient as compared to standard FEM [48]. Additionally, DG FEM allows non-conformal mapping along interfaces. In other words, we can mesh different sections of the domains with dissimilar mesh densities with non-matching interfaces, which is particularly beneficial since the minimum element sizes vary across different domains. The polynomials used for interpolation in DGM are also higher order (4th to 6th order), resulting in smaller models (i.e., fewer degrees of freedom as compared to standard FE models).

The DGM method solves the elastic wave equation in velocity–strain formulation rather than the standard displacement field described in Eq. (2). Thus, to obtain the displacement field, we have to integrate the velocity field with respect to time. In DGM, the governing equations for elastic wave propagation in the absence of body forces (equivalent to Eq. (2)) take the form

$$\rho_s \frac{\partial \boldsymbol{v}_s}{\partial t} - \nabla \cdot \boldsymbol{\sigma} = \boldsymbol{0},$$
$$\frac{\partial \boldsymbol{\epsilon}}{\partial t} - \frac{1}{2}\left[\nabla \boldsymbol{v}_s + (\nabla \boldsymbol{v}_s)^{\mathsf{T}}\right] = \boldsymbol{0}, \tag{8}$$

where $\boldsymbol{v}_s$ is the particle velocity. In the fluid domain, linearized Euler equations (continuity and momentum equations) are solved, where the dependent variables are the fluid pressure and the particle velocity (also called acoustic velocity perturbation). The acoustic wave equation in the absence of body forces takes the form

$$\frac{1}{\rho_f c_f^2} \frac{\partial p_t}{\partial t} + \nabla \cdot \boldsymbol{v}_f = 0,$$
$$\rho_f \frac{\partial \boldsymbol{v}_f}{\partial t} + \nabla \cdot (p_t \boldsymbol{I}) = \boldsymbol{0}, \tag{9}$$

where p_t is the total acoustic pressure, $\boldsymbol{v}_f$ is the total acoustic velocity, c_f is the speed of sound in the fluid, and $\boldsymbol{I}$ is the identity matrix. The interface conditions are similar to Eqs. (4)–(6) (continuity in displacement, velocity, and normal stresses across interfaces), while the boundary condition is also similar to Eq. (7), where the displacement $\boldsymbol{u}$ is replaced by the velocity $\boldsymbol{v}_s$, i.e., $\boldsymbol{v}_s(\boldsymbol{l}, t) = \bar{\boldsymbol{v}}_s g(t)$.

Using DGM, we perform time-dependent analyses on the clamp-on system geometry shown in Fig. 2(b) to identify different wave profiles. The wave interactions in the complete clamp-on system are very complex, so it is difficult to distinguish different types of waves and their interactions throughout the domain. Thus, we characterize these waves by segmenting the clamp-on geometry into different sections, such as wedge-pipe wall and pipe wall–fluid portions. Additionally, the pipe wall is a thin region compared to the wedge and the water domains in contact, which makes it challenging to visualize the wavefield in the pipe wall. Thus, we modify the geometry (only for identifying the wavefields) as shown in Fig. 3(a), where the pipe wall dimensions are comparable to the wedge (width of 36 mm and height of 22.5 mm). We apply Dirichlet BC on the slant face of the wedge along the brown dashed line as shown in the same figure (similar to Fig. 1(b)). Since the incident pulse is a P wave, we prescribe the velocity normal to

the edge and perform the time-dependent analysis. We select the time step as $t_s = T/15$, where $T = 1/f$ is the time period of the input signal ($f = 1\,\text{MHz}$), while we set the total simulation time $20 \times T$. Fig. 3(a) shows the velocity profile of the wedge-pipe wall system at approximately $t = 12 \times T$, where we can see the reflected and transmitted pulses with plane wavefronts and additional waves with circular wavefronts.

Similarly, we conduct the time-dependent analysis of the pipe wall–fluid system, where the same time step ($T/15$) is used, while the total simulation time is modified to $15 \times T$ to reduce reflections from free edges. As in the case of the wedge-pipe wall system, we modify the pipe wall–fluid system's geometry for better visualization of the waves present (refer to Fig. 3(d)). Here both the solid and fluid domains are 50 mm wide, while the fluid region is 30 mm high, whereas the pipe wall has a 31.3 mm height. Additionally, the edge of the pipe wall where the incoming signal comes from (left edge in Fig. 3(d)) is also modified to match the angle of the incoming S wave (52.4°). Then we prescribe the Dirichlet BC along the brown dashed line, where the direction of the velocity is parallel to the edge (to match the behavior of the S wave). The resulting velocity profile shown in Fig. 3(d) displays both the S wave in the pipe wall (reflected from the pipe wall–fluid interface) and the P wave transmitted to the fluid. Using these two velocity profiles, we can measure the reflection and transmission angles of the wedge-pipe wall and pipe wall–fluid interfaces, which can be compared against the theoretical predictions (angles ϕ_1, ϕ_2, and ϕ_3 discussed in Section 2.1).

2.3. Comparison between ray tracing and DGM

To verify the accuracy of the DGM models in predicting the wave propagation behavior of the clamp-on UF, the propagating angles are compared with theoretical (ray tracing) predictions. These DGM models also allow us to investigate the presence of additional waves in the clamp-on UF, which is not possible via ray tracing. Since the time-domain analysis provides us with a resultant field (velocity in the solid domain and velocity/pressure in the fluid region), it would be insightful to discriminate the wave behavior into S and P waves. To that end, we use a wavefield decomposition method.

2.3.1. Wavefield decomposition

We perform the wavefield decomposition whereby the resultant velocity field is decomposed into a scalar (for P waves) and a vector (for S waves) field. This decomposition is carried out by wave-type separation using dilation and rotation calculations, where the wavefield is represented as a combination of irrotational (curl-free) and solenoidal (divergence-free) fields [49]. Although there are other methods, such as Helmholtz decomposition [50], which preserve the amplitude and dimension of the field variables, they are more complicated to implement. As spatial derivatives are used in the process, the separated field contains one less spatial dimension than the original one. In other words, a velocity field with the dimension m/s transforms to a field with a dimension of 1/s. However, we are interested only in the different types of waves, their propagation angles, and their wavefronts' shapes, and not in the exact amplitude of the waves; a qualitative analysis such as the wave-type separation is sufficient.

For the separation of fields, we consider a velocity field $\boldsymbol{v}(\boldsymbol{x}, t) \in \mathbb{R}^2$, where $\boldsymbol{v}$ can be written as:

$$\boldsymbol{v} = -\nabla \psi + \nabla \times \boldsymbol{A}, \tag{10}$$

where ψ is the scalar potential and $\boldsymbol{A}$ is the vector potential. Since P waves are irrotational, the curl of $\boldsymbol{v}$ removes them and produces only S waves. Similarly, S waves are solenoidal, and the divergence of $\boldsymbol{v}$ provides only P waves. We apply wave-type separation to all segments of the clamp-on system, as described next.

2.3.2. Wedge-pipe wall interface

The first section of the clamp-on UF that we compare (between ray tracing and DGM) is the wedge-pipe wall interface (transmitter side) – left wedge from Fig. 2(b), where the plane incident P wave interacts with the solid–solid interface to produce a transmitted P wave, and two reflected (P and S) waves. From the resultant wavefield (Fig. 3(a)), it is not instantly apparent that S waves are also reflected, which can be clearly visualized in the decomposed field (see Fig. 3(c)). In the separated fields (Figs. 3(b) and 3(c)), we have also marked angles of different plane waves along with their polarization. The reflected P wave travels back to the wedge at the incident angle ($\phi_1^P = \phi_1 = 30°$), while the reflected S wave is at $\phi_1^S = 17.6°$. The S wave transmitting to the pipe wall is marked in Fig. 3(c) as $\phi_2^S = \phi_2 = 52.4°$. Since ϕ_1 is greater than the first critical angle, we do not expect any P waves in the pipe wall. Fig. 3(b) shows that, indeed there are no plane P waves traveling through the pipe wall. All the aforementioned angles (ϕ_1^P, ϕ_1^S, ϕ_2^S) are consistent with Snell's law predictions.

Figs. 3(a)–(c) also show additional waves that ray tracing could not predict because of its inherent limitations (plane wavefront in a semi-infinite domain). For instance, when the incident angle is larger than the critical angle, waves do not propagate through the second medium according to the ray approximation. However, we can see in Fig. 3(b) an evanescent P wave traveling along the wedge-pipe wall interface that enters the pipe wall with a cylindrical wavefront. Additionally, the reflected P wave proceeds towards the free surface of the wedge, which then reflects back into the wedge, resulting in several P waves with cylindrical wavefronts. Similarly, many S waves with cylindrical wavefronts are also present, as can be seen in Fig. 3(c). These are generated due to the point-source nature of the edges of the plane wavefront. In addition, the P waves with the cylindrical wavefront that are reflected from the interface towards the slant edge of the wedge reflect to form another S wave with a plane wavefront. This new plane S wave is also at ϕ_1^S angle with the normal to the slant edge, which travels to the wedge-pipe wall interface at an angle $2 \times \phi_1^S$. All the aforementioned signals and noise of both P and S type travel to the pipe wall, and some portions of their energy enter the measuring fluid.
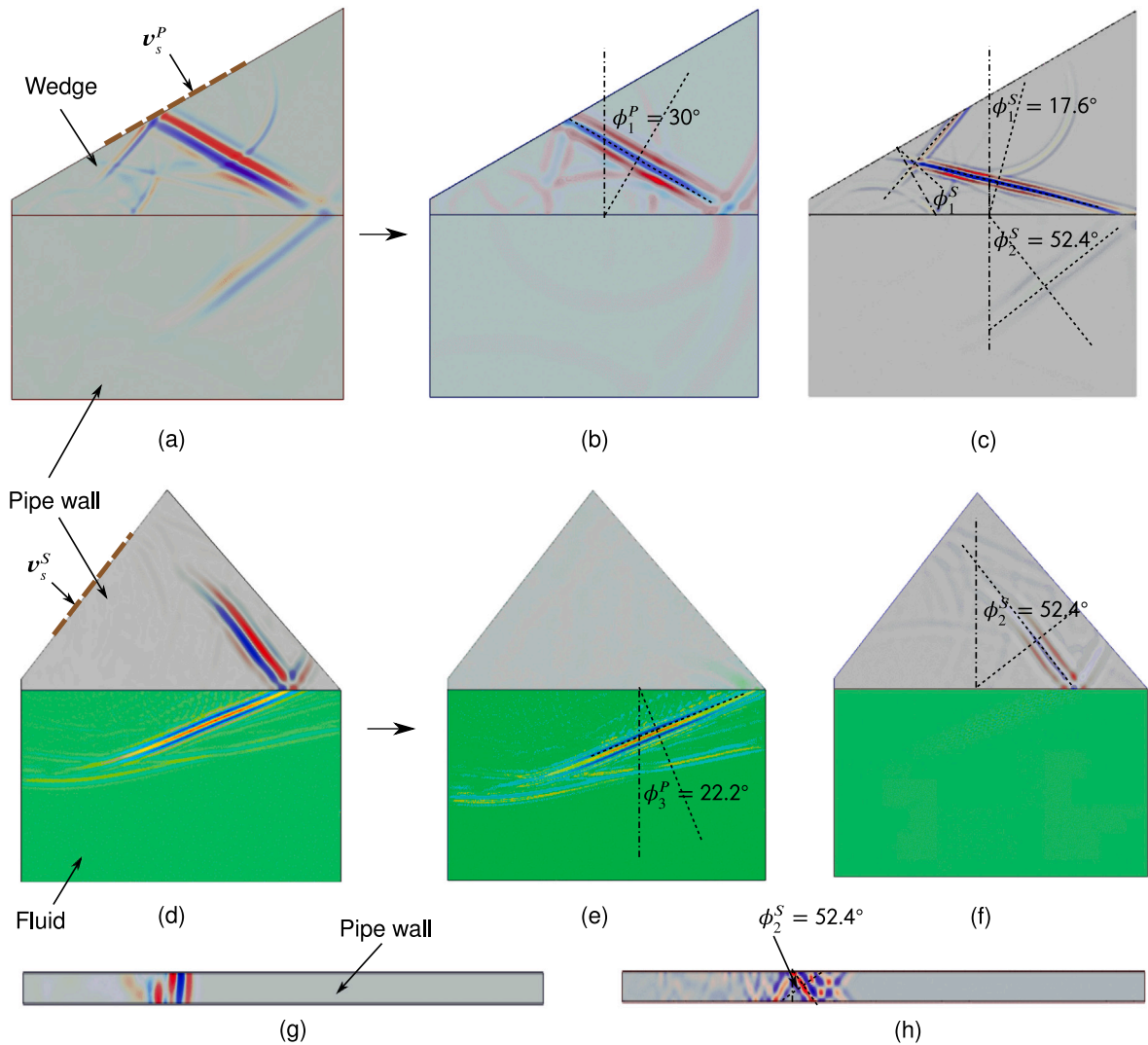
Fig. 3. Decomposition of the wave field into P and S waves. (a) and (d) are, respectively, velocity fields of the wedge-pipe wall and pipe wall–fluid interfaces. The former is a solid–solid interface, while the latter is a solid–fluid interface where the incident prescribed velocity BCs ($\boldsymbol{v}_s^P$ and $\boldsymbol{v}_s^S$) are marked using brown dashed lines. (b) and (e) are the corresponding P wavefields, where ϕ_1^P represents the angle of reflection of the incident P wave from the interface and ϕ_3^P is the transmission angle to the fluid. (c) and (f) are S wavefields of (a) and (d), respectively, where ϕ_1^S and ϕ_2^S are the reflected S wave angle to the wedge and the transmitted S wave angle to the pipe wall. ϕ_1^S marked close to the slant face of the wedge is the secondary reflected S wave due to the reflected P wave. (g) and (h), respectively, represent the P and S wavefield of the pipe wall for the entire simulation (150 cycles) where ϕ_2^S is the same as in (f) and (c). As shown in (g), no specific angles are present for P waves in the pipe wall.

2.3.3. Pipe wall–fluid interface

The next section of the clamp-on system is the pipe wall–fluid interface, which is a solid–fluid interface and has a more complicated wave propagation behavior than the solid–solid interface. This is because waves can travel through solid, fluid, and their interface. The resultant velocity field, along with its decomposition (in P and S waves), are provided in Figs. 3(d)–(f). At the pipe wall–fluid interface, the incoming primary S wave (at $\phi_2^S = 52.4°$) generates the required P wave in the fluid (at $\phi_3^P = 22.2°$) that has a plane wavefront as marked in Fig. 3(e). This S wave is also reflected through the wall to become the first noise signal that also has a plane wavefront (except for the edges with circular wavefront) as shown in Fig. 3(f).

Similar to the previous section, we can observe several S waves with cylindrical wavefronts in the pipe wall that transmit energy to the fluid at different intervals. Also, noise signals are present in the fluid domain (P-type) at different angles generated due to the point source nature of the wavefront's edges. Noteworthy, the different noise waves entering from the wedge-pipe wall section are not shown here since prescribing all those disturbances as BCs is nearly impossible. However, all these waves are present in the complete clamp-on UF simulation performed for the actual geometry (Fig. 2(b).)

Snapshots of P and S waves in the pipe wall from a complete clamp-on system simulation are, respectively, shown in Figs. 3(g) and 3(h). The pipe wall's length is selected as 140 mm and the total simulation time as $t_S = 150 \times T$. We used the same time step

($T/15$) as in previous simulations for the clamp-on model. As shown in Fig. 3(h), the primary S wave travels through the pipe wall with a planar wavefront at an angle ϕ_2^S, while some noise S waves travel without any specific angle. All P waves propagate with a cylindrical wavefront (the small lateral dimension of the pipe wall makes it look like a flat wavefront), as shown in Fig. 3(g). The superposition of the P and S wavefields provides the total wavefield in the pipe wall, which looks similar to the schematic representation of the wavefield in the pipe wall region of Fig. 2(b). All the animations (traveling waves) corresponding to Fig. 3(a) – 3(h) are provided in the supplementary material, Section 0.2. The complete simulation of the clamp-on UF also shows that noise signals (P and S) are present throughout the simulation time, which must be removed to distinguish the required signal from the fluid. To that end, we need to understand all waves in the clamp-on UF and categorize them based on their wavefront shape and behavior, discussed in the next section.

2.4. Types of waves present in the clamp-on system: Ideal vs. non-ideal waves

We have seen previously in Fig. 3 that P and S waves are present in the wedge, pipe wall, and their interface, while the fluid contains only P waves. We have also observed that some of these waves have planar wavefronts while others possess cylindrical wavefronts, so we categorize them according to their behavior and origin. The waves with planar wavefronts that propagate with the angles predicted by Snell's law (ray acoustics), such as primary P and S waves in the wedge, are *ideal waves*: their travel time and direction can be calculated straightforwardly (for a pipe with a static fluid). However, for Snell's law to be completely valid, the media at either side of the interface must be semi-infinite, or the wavelength should be very small compared to the characteristic length. Since none of the domains (wedge, pipe wall, and water) are semi-infinite, there will always be portions of the wave energy that do not follow Snell's law, such as the curvatures at the ends of the plane wavefronts. These waves with cylindrical wavefronts are generated due to the point-source nature of the source and interactions of oblique waves with multiple interfaces; we call them *non-ideal waves*. For instance, the secondary P wave with the cylindrical wavefront in the wedge is a non-ideal wave with no specific direction of propagation (see Fig. 3(c)). These non-ideal waves are present predominantly in the pipe wall region, which is a thin section with relatively high impedance where the incoming wavelength is comparable to the wall thickness. This is further aggravated due to the presence of both solid–solid (wedge-pipe wall) and solid–fluid (pipe wall–fluid) interfaces. As non-ideal waves are present throughout the simulation, determining their arrival time or direction is cumbersome. Additionally, since these waves can interact with the ideal waves, they could produce more unpredictable disturbances in the measurement process.

Similarly to the wedge and pipe wall, the primary wave (working signal) in the fluid region is an ideal wave, as represented using blue arrows in Fig. 2(b). Since the primary S wave reflected from the pipe wall–fluid interface travels through the pipe wall to reach the receiving wedge with a plane wavefront, it is also an ideal wave. Since the working signal has to travel through the pipe wall from the fluid, it also transforms into an S wave, which travels at the same angle ($\phi_2 = 52.4°$) as the primary S wave in the pipe wall (as represented using blue and red arrows in the receiving wedge in Fig. 2(b)). Since these two ideal waves (working signal and primary S wave in the pipe wall) have the same incident angle, polarization, and frequency, it becomes difficult to distinguish them based on the aforementioned aspects. However, the reflected primary S wave has a higher wave speed (refer Table 1) and shorter travel distance than the working signal, so it reaches the receiver much earlier than the P wave from the fluid. Since this wave is separated from the working signal it does not cause crosstalk. Similar to the working signal, we can accurately determine the arrival time of this S wave for a clamp-on UF with a static fluid setting. However, this primary S wave can reflect back to the pipe wall from the receiver, which can take multiple paths traveling around the pipe wall, resulting in a "ringing" that adds more noise to the measurement. The non-ideal signals in the fluid are generated due to multiple interactions between the waves in the pipe wall and the fluid and have several wave paths. Since they also possess the same frequencies as the working signal, it is difficult to distinguish them.

All signals (ideal and non-ideal, P and S) that reach the receiving piezo transducer are represented using a time series, where voltages (corresponding to the displacements) are recorded for a definite time period. Since we can predict the travel time of the working signal and primary noise signal (ideal S wave through the pipe wall), we can mark them in the time series and filter the latter by time-windowing. However, as the non-ideal waves are present throughout the time spectrum, we cannot filter them *a posteriori* by standard means, such as using frequency band filtering or time windowing. Additionally, as the working signal and noise signals are coming through the same interface, it is virtually impossible to apply conventional vibration isolation systems at the receiver to remove the noise, as it will affect both the working signal and noise equally. So, we need to develop a noise mitigation mechanism that can alleviate these non-ideal noise signals from the output time series to distinguish the working signal and improve the measurement accuracy. To that end, we need a filtering mechanism that can minimize the generation of noise signals and is sensitive to specific directions and frequencies that align with the working signal. In addition, both wedges should ensure optimal energy transfer and maintain the shape of the wavefront since a distorted wavefront will lose the plane wave nature and directionality and thus disturb the measurement and may not be detected by the receiver. Moreover, as the arrival time of the working signal is relevant in the clamp-on system, the filters should particularly attenuate noise close to the required signal in the time domain. We can potentially achieve these by using PnCs.

3. Phononic crystals for noise attenuation

Since PnCs have been used for wave manipulation (wave suppression, steering, focusing, and cloaking), we explore their capabilities in mitigating noise for the clamp-on UF. Fig. 4(a) shows the schematic of a single phase 2D PnC's periodic unit cell (PUC) comprised of solid material, with its irreducible Brillouin zone (IBZ) $\Gamma - X - M - \Gamma - M'$ and lattice vectors $\boldsymbol{a}_i$, $i = \{1, 2\}$. The
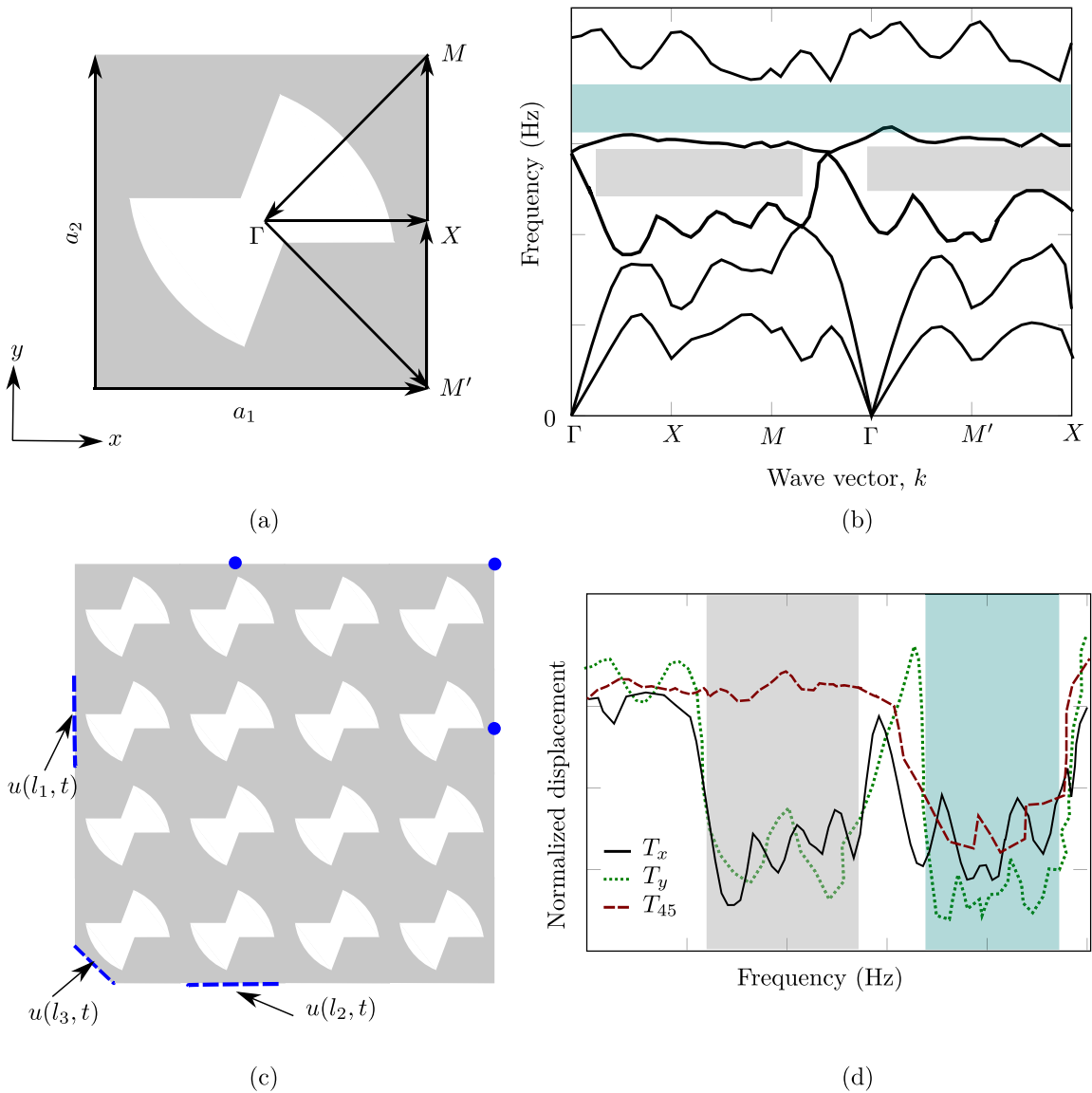
Fig. 4. (a) Schematic of a PUC of the 2D PnC with its IBZ; (b) Band structure of the PUC, i.e., frequency as a function of the wave vector, where the teal-shaded region shows a complete BG and gray-shaded regions represent partial BGs. (c) waveguide composed of a 4X4 array of the PUC, where Dirichlet BCs are prescribed on the edges using blue dashed lines while output displacements are measured at blue dots. (d) transmissibility relations (along *x*, *y*, and 45°) represented as the ratio of the output displacement (measured at the opposite side of the prescribed displacement) to the prescribed input displacement as a function of the supplied frequency, where partial and complete BGs are shaded using gray and teal regions.

PUC is the repeating unit of the PnC, whereas the IBZ is the smallest section that can represent the Brillouin zone that is obtained by transforming the PUC from direct lattice (Bravais lattice) to the reciprocal lattice [51]. The wave propagation behavior of the PnC's PUC is characterized using a band structure as discussed next.

The band structure or dispersion relation [52] is the relation between the applied frequency and the wave vector *k* (whose amplitude is the reciprocal of the wavelength and whose direction is the direction of wave propagation [52]). The band structure can be used to reveal a complete or partial bandgap as described in Fig. 4(b), which shows the schematic of a band structure. In this figure, different bands (curves) describe traveling waves, while the slopes of these bands capture their propagation speed. The teal-shaded region, where wavebands are absent, indicates a complete BG, where waves experience omnidirectional attenuation for all wave vector values. The gray-shaded regions in the same figure show partial BGs, which do not span the entire IBZ. In other words, for the same frequency range, wavebands are present in the $M - \Gamma$ branch; thus, waves propagate for *k* corresponding to 45° orientation while they are attenuated for *k* along *x* and *y* directions due to lack of wavebands in those IBZ branches. Hence, partial BGs enable the PnCs to possess directional wave propagation characteristics, and will be termed directional BGs (DBGs) hereafter.

Since we want to design a structure that allows waves to propagate in certain directions while suppressing them in other directions, we explore possibilities of using devices possessing DBGs. DBGs are generally not present in a PUC with a complete symmetry (8-fold symmetry in 2D that has a triangular IBZ) because of the presence of symmetric modes; thus, we need to introduce asymmetries in the band structure by tuning the PUC geometry. Hence, the PUC in Fig. 4(a) has a 4-fold symmetry thereby possessing more IBZ branches (5 branches in total) than a completely symmetric PUC (IBZ with 3 branches). This leads to the increased computational cost for the band structure analysis. In the following, we discuss the different analyses used to design PnCs with DBGs that can act as directional wave filters for the clamp-on system.

3.1. Analysis of PnCs with DBGs

For the waveguiding application in clamp-on flowmeters, we consider a single phase 2D PnC composed solely of solid material, so we can use the same elastic wave Eq. (2) to describe the wave propagation through the PnC. We still need to provide appropriate BCs to the boundary value problems (BVPs); we study two BCs as discussed next.

3.1.1. BVP1: Band structure analysis

The first analysis we perform is the band structure analysis obtained by conducting a set of eigenvalue analyses of the PUC after applying Bloch-Floquet periodic boundary conditions (BFPBCs) [53] and sweeping the wave vector through the vertices of the IBZ as shown in Fig. 4(a). The BFPBC takes the form:

$$u(x + a_i, t) = e^{ik.a_i} u(x, t), \tag{11}$$

where i is the imaginary number. The magnitudes of the lattice parameters (Fig. 4(a)) are equal for the square PUC, i.e.,

$$\|a_1\| = \|a_2\| = a, \tag{12}$$

where a is the magnitude of the lattice vector in both directions. Although the band structure analysis reveals the presence of BGs and DBGs (frequency and wave vector ranges), it does not provide actual wave propagation behavior of the PnC structure comprised of a finite number of PUCs. This is because the band structure analysis assumes an infinite medium due to the application of BFPBCs. Thus, we conduct a transmissibility analysis over a finite PnC waveguide to obtain its performance.

3.1.2. BVP2: Transmissibility analysis

Transmissibility analysis or harmonic frequency sweep analysis [54] is the steady-state frequency response analysis of the finite PnC waveguide from Fig. 4(c) after applying essential (or Dirichlet) BCs [55] for the range of applied frequencies. For a given frequency, the transmissibility relation provides the transmission amplitude of the traveling wave in the finite PnC waveguide. We perform three transmissibility analyses by providing Dirichlet BCs along three different directions, as shown in the figure, to investigate the wave propagation at 0°, 90°, and 45° orientations. These BCs are similar to the one defined in Eq. (7), except that in PnC analyses, we assume a time-invariant harmonic response. The expressions take the form:

$$u(l_1, t) = \bar{u}_1 e^{i\omega t} \underline{e}_1 \qquad u(l_2, t) = \bar{u}_2 e^{i\omega t} \underline{e}_2 \qquad u(l_3, t) = \bar{u}_3 e^{i\omega t} \left(\underline{e}_1 + \underline{e}_2 \right), \tag{13}$$

where $\bar{u}_1$, $\bar{u}_2$, and $\bar{u}_3$ are constant displacement amplitudes applied along $x = l_1$, $x = l_2$, and $x = l_3$, respectively, while ω is the applied angular frequency in rad/s. $\underline{e}_1$ and $\underline{e}_2$ are the unit vectors in x and y directions, respectively. The displacements in the three orientations are measured at the blue dots in the figure, opposite to the Dirichlet BC region, and are divided by incident displacement amplitudes to obtain transmissibilities T_x, T_y, and T_{45}. Since the waves are suppressed within the BG, the displacement amplitude there would be significantly lower than outside the BG. When the PnC waveguide possesses a DBG, depending upon the direction of the wave propagation (given by the Dirichlet BC as shown in Fig. 4(c)), the transmissibility shows either an attenuation, propagation, or combination response thereof. Fig. 4(d) shows the schematic of the transmissibility relations T_x, T_y, and T_{45}, where the complete (teal) and partial (gray) BGs from the band structure (Fig. 4(b)) are also shown. We can observe that T_{45} experiences little attenuation within the DBG frequency range while T_x and T_y are immensely suppressed, corroborating the directional propagation property of the PnC waveguide. Additionally, since the transmissibility analysis provides the attenuation rate within the BG, we can select the number of PUCs in the PnC waveguide, depending on the required wave attenuation (more PUCs along the propagation direction lead to a higher reduction in amplitude). In addition, as the transmissibility response can be obtained for different locations, we can determine an adequate arrangement pattern of the PUCs within the DBG PnC waveguide for its optimal performance in the clamp-on flowmeter application.

3.2. Design of the directional BG PnC's periodic unit cell and waveguide

Using the aforementioned analysis techniques, we design the PUC and the waveguide of the directional BG PnC. Since the BG is generated by Bragg scattering, the magnitude of the lattice vector a is related to the applied frequency via the Bragg law of diffraction [21]. We select PSU (the wedge material) for the PnC as well, and we calculate a using PSU's wave speeds from Table 1 and the required frequency (1 MHz) as:

$$n\lambda = 2a \cos\theta, \qquad \lambda = c/f, \tag{14}$$

where n is an integer (generally $n = 1$), λ is the wavelength of the applied wave in the material, θ is the angle of incidence of the wave to the normal of the surface, and f is the applied frequency. Supplying the aforementioned values to Eq. (14) provides us with
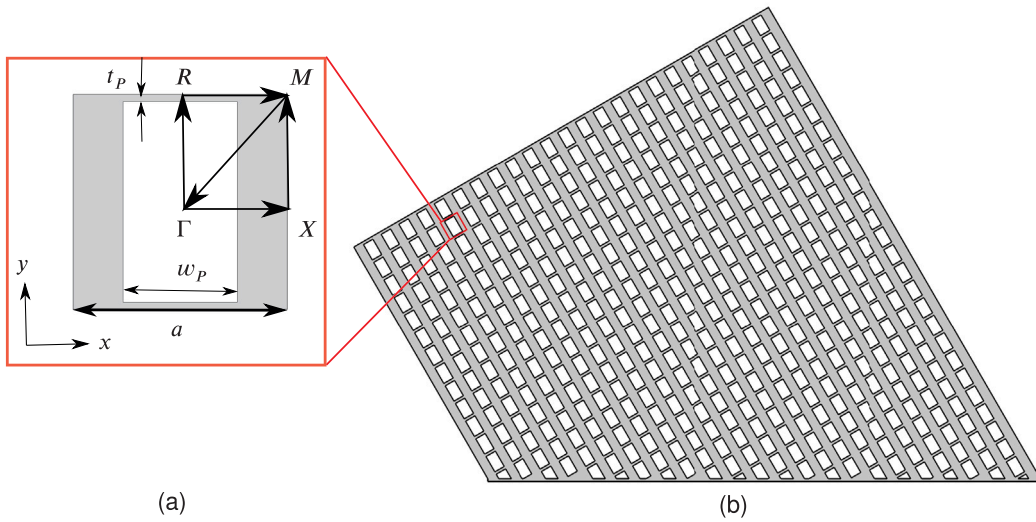
Fig. 5. (a) 2D directional BG PUC with IBZ $\Gamma - X - M - \Gamma - R - M$, where a is its lattice vectors' length, and the two additional parameters w_P and t_P defining the geometry. (b) the design of the PnC wedge with 492 DBG PUCs, whose edges are also reshaped to reduce wave reflections to the measuring region. The two parallel edges of the wedge also sit at 30° with the vertical.

$a = 0.75$ mm. Since we need to introduce asymmetries to generate DBGs, we employ an anisotropic material distribution in the PUC (as shown in Fig. 5(a)), thereby increasing the stiffness and mass towards the y direction more than in the x direction. Further, we follow the displacement-mode-based analysis discussed in our previous work [56], whereby the desired band structure is achieved by modifying the relevant displacement modes bounding the wavebands via tuning the PUC geometry. Thus, we arrive at a PUC design possessing a directional BG in the x-direction in Fig. 5(a). The dimensions of the PUC are also marked in the figure, where the thickness of the thinnest section is $t_P = 0.05$ mm, and the width of the void region is $w_P = 0.4$ mm. As apparent from the PUC geometry, the thickness of each layer in the y-direction is 3.5 times larger than that of the x-direction. Therefore, waves traveling in the y-direction experience less resistance than in the x-direction.

After designing the PUC with directional BGs in the required frequency range and direction, we develop the PnC waveguide in the form of a wedge similar to the wedge from the initial clamp-on flowmeter (Fig. 2) to create the transmitter and receiver. Since the vertical edge of this wedge (a free surface) can reflect waves back to the measuring region, we reshape the wedge to induce a larger reflection angle, thereby guiding the noise signals away from the measuring domain. Similarly, the portion of the wedge opposite to the vertical edge is a small region in contact with the pipe wall and can also contribute more noise to the system; hence, it is also modified. Then, the PnCs are added to the modified wedge to transmit the required signal in the desired direction by rotating the PnC waveguide 30° (wedge angle) from the y-axis as shown in Fig. 5(b). The resulting PnC wedge is a trapezium with 24 PUCs arrayed between its parallel edges (along the local x-axis), while the short and long sides have 14 and 27 PUCs, respectively. Thus, in total, the wedge has 492 directional BG PUCs. We use the same geometry for transmitting and receiving wedges to allow the reciprocity necessary for the transit-time flow measurement application. Further, we verify the performance of the PUC and waveguide by band structure and transmissibility calculations.

3.2.1. Band structure response of directional BG PnC

We obtain the band structure of the 2D square PUC in Fig. 5(a) by using the $\omega(\mathbf{k})$ approach, whereby the frequencies are calculated as a function of $\mathbf{k}$ values sampled through the IBZ [57]. Recall that since BFPBCs are applied, the band structure analysis assumes an infinite material. We consider the square PUC with a 4-fold symmetry; thus, the shape of the IBZ is a square with one diagonal (both PUC and the IBZ are shown in Fig. 5(a)). Fig. 6(a) shows the band structure of the PUC with shaded directional BGs. The inset in the figure shows the Brillouin zone and the IBZ of the PUC. The normalized wave vector shown in the x-axis is obtained after multiplying the wave vector $\mathbf{k}$ with the lattice length a. There are six wavebands present in the band structure between 0 and 2 MHz that span five branches of the IBZ, and we use 5000 wave vector steps (1000 steps per branch) to represent these branches. The directional BGs bounding frequencies f_1 through f_{16} are also marked in the figure.

Fig. 6(b) shows a tabular description of the BG frequency ranges, their bounding wavebands, and corresponding IBZ branches. It shows that BGs are only present in the $\Gamma - X$ and $R - M$ branches of the IBZ. For the remaining branches ($X - M$, $M - \Gamma$, and $\Gamma - R$), wavebands are present throughout the frequency range, implying the absence of BGs for waves traveling towards the y-direction and 45° orientation (both local to the PUC coordinate system). We can also observe that more BGs are present in the $R - M$ branch, and corresponding wavebands experience a larger spread compared to the $\Gamma - X$ branch. This is because the first IBZ branch contains only wave vectors in x-direction while the latter also possesses a non-zero y component; thus, more waves are allowed to propagate through the $R - M$ branch. Once we obtain the DBG frequency ranges and corresponding IBZ branches, we move towards the transmissibility analysis to attain the performance of the finite PnC waveguide.
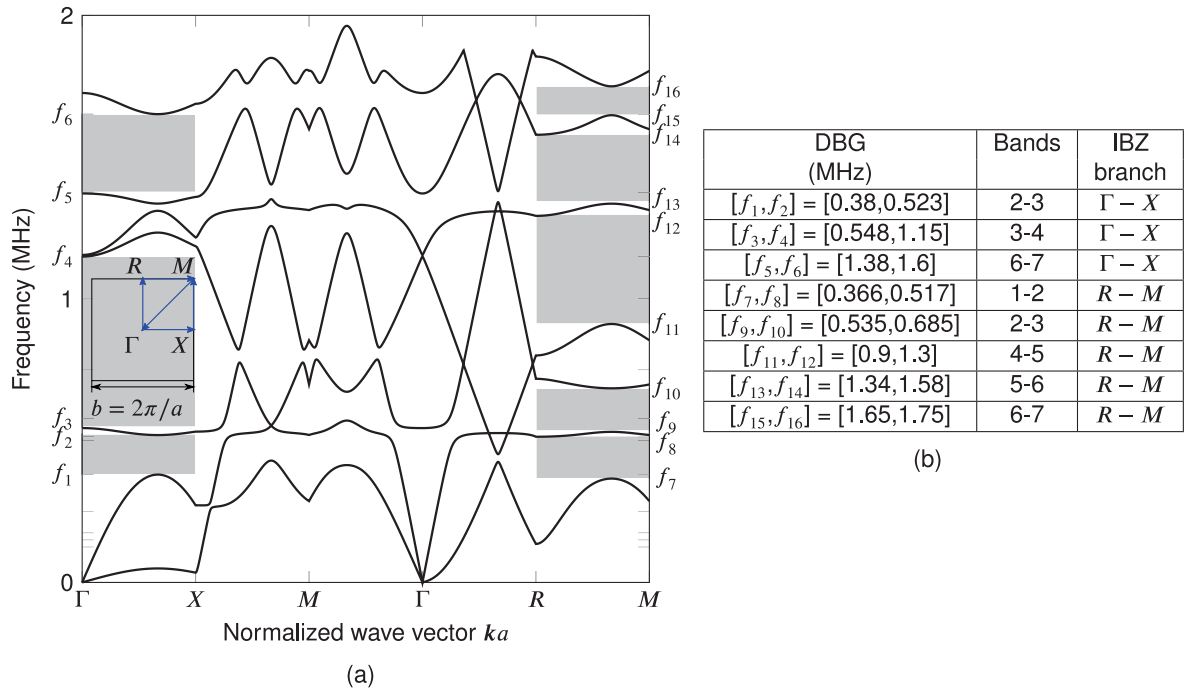
DBG (MHz)	Bands	IBZ branch
$[f_1, f_2] = [0.38, 0.523]$	2-3	$\Gamma - X$
$[f_3, f_4] = [0.548, 1.15]$	3-4	$\Gamma - X$
$[f_5, f_6] = [1.38, 1.6]$	6-7	$\Gamma - X$
$[f_7, f_8] = [0.366, 0.517]$	1-2	$R - M$
$[f_9, f_{10}] = [0.535, 0.685]$	2-3	$R - M$
$[f_{11}, f_{12}] = [0.9, 1.3]$	4-5	$R - M$
$[f_{13}, f_{14}] = [1.34, 1.58]$	5-6	$R - M$
$[f_{15}, f_{16}] = [1.65, 1.75]$	6-7	$R - M$

(b)

Fig. 6. (a) Band structure of the 2D PnC PUC with the inset showing a square BZ of the dimension $b = 2\pi/a$ where the IBZ is marked with blue arrows and the shaded regions represent DBGs. (b) Table listing the directional BG frequency ranges, their enclosing wavebands, and the IBZ branches, which shows that BGs are only present in $\Gamma - X$ and $R - M$ branches.

3.2.2. Transmissibility response of the finite PnC waveguide

Transmissibility analyses are performed for the PnC waveguide after applying Dirichlet BCs, as shown in Fig. 7(a), where the waveguide is composed of a 5×5 PUC array. Noteworthy, the PUC at the left bottom of the waveguide is replaced by a 45° wedge to provide the essential BC $u(l_3, t)$ at 45°. The analyses are conducted for the frequency range 300 kHz to 1.8 MHz (the range includes all DBGs) with a frequency step of 10 kHz and an input amplitude of 1 μm. A low-reflective BC is applied along the remaining edges of the waveguide to minimize reflections from free edges. As discussed in Section 3.1, output displacements are measured opposite to the prescribed BC (blue dots), and transmissibility responses are obtained towards x, y, and 45° directions and shown in Fig. 7(b). Noteworthy, we positioned the probing point corresponding to the 45° to keep consistent the distance between the location of the BC to the probing point (distance of 3.75 mm) for all three transmissibility cases.

In Fig. 6(b), T_x, T_y, and T_{45}, respectively, represent the transmissibility towards x, y, and 45° directions. The shaded regions in the plot show overlapped BG frequency ranges predicted by the band structure analysis along the $\Gamma - X$ and $R - M$ branches of the IBZ (no BGs are present in other IBZ branches). Within the BG frequency range, towards x-direction, waves experience an immense attenuation with an average attenuation rate of 10^{-5} (see red solid curve), while towards y-direction, the waveguide exhibits a smooth transmission similar to the wave propagation through a uniform structure such as a bar or a beam (see blue dotted curve); thus we can say that the waves traveling in y-direction experience negligible attenuation. Wave propagation towards 45° (green dashed curve) is close to T_y but does not exhibit the same response. This is because it is nearly impossible to excite the PnC waveguide at 45° without influencing modes in x and y directions. Thus we observe a moderate attenuation (average 2×10^{-2}) in the 45° direction.

Since we want to guide the input signal through a specific path via the wedge to the pipe wall while minimizing noise generation, we incorporate the PnC waveguide to the wedge as shown in Fig. 5(b). As mentioned before, we orient the waveguide such that the vertical side of the PUC ($X - M$ branch of the IBZ) aligns with the desired P wave propagation angle of 30° to the wedge, thus allowing a complete transmission of the input signal. This orientation also ensures that waves traveling in other directions are attenuated, and only a small fraction enters the pipe wall. After performing the transmissibility analysis of the PnC waveguide and designing the wedge, we proceed to the analysis of the complete clamp-on UF.

3.3. Comparison of clamp-on system with and without directional band gap PnC

Noise levels in the pipe wall, the time response at the receiving wedge, and the frequency content of the receiving signal are compared between the standard clamp-on system and the one possessing directional BG PnC wedges to check the performance of the added PnC structure. In the 2D model of the clamp-on system, the standard wedges of the existing clamp-on geometry from
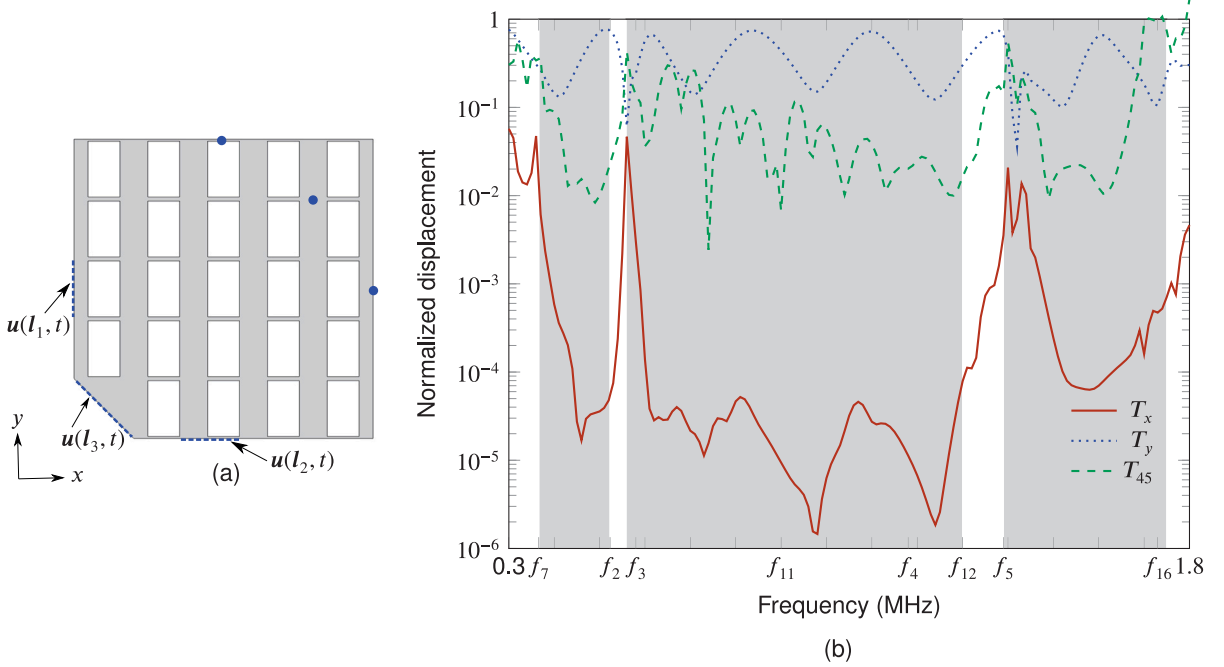
Fig. 7. Transmissibility relation of the 2D PnC waveguide for different directions, where (a) the PnC waveguide geometry marked with Dirichlet BCs and probing points. (b) the transmissibility response: the normalized displacement (in log scale) as a function of the applied frequency in MHz, where BGs predicted by the band structure are shaded (marked with f_7, f_2, f_3, f_4, f_{11}, f_{12}, f_5, and f_{16}). Transmissibility in x-direction, T_x is represented using the solid red curve that has a low amplitude (average 10^{-5}), while the blue dotted curve shows the transmissibility in y-direction and its amplitude is close to 1. Transmissibility along $45°$, T_{45} is shown using green dashed line and is between T_x and T_y.

Fig. 2(b) are replaced with the PnC wedges from Fig. 5(b). Wave propagation analysis through the updated clamp-on system is carried out similarly to the standard one (refer to Section 2.2).

Since the different media of the clamp-on flowmeter have different field variables, to compare the performances of the PnC-embedded clamp-on design with the standard one, we select the pressure profile of the complete system and displacement at the center of the receiving wedge's slant face as parameters. The former provides information about the traveling waves, including the required signal and noise in the entire system, whereas the latter shows the influence of the PnC waveguide in the signal and noise amplitudes at the receiver.

3.3.1. Pressure profile and displacement comparison

Fig. 8 displays the comparison between the original (top) and PnC (bottom) versions. Figs. 8(a) and (c) show snapshots of pressure profiles corresponding to the time ($120\,\mu s$) when the resulting signal from the fluid is about to impinge the pipe wall. This time interval is particularly relevant because this is the time for which we need to minimize the noise amplitude to get an accurate measurement. From pressure profiles, we observe a considerable amount of noise in the pipe wall of the clamp-on system with the standard wedge as compared to the PnC counterpart. In addition, the fluid region of the standard clamp-on design also exhibits higher wave scattering than the one with PnC-embedded wedges, implying that the noise signals from the pipe wall induce more noise in the fluid. Thus, we can state that the PnC waveguide is filtering most of the noise signals from the pipe wall and the fluid, consequently aiding in identifying the required signal at the receiver.

The displacement response on a point along the slant edge of the receiving wedge, as marked in Figs. 8(a) and (c), is compared next. Since the independent variable in DGM analysis is velocity, we extract velocities in x and y directions, which are then integrated to obtain their corresponding displacements. Then, by using the component addition, the resultant displacement normal to the edge of the wedge is

$$u_{res} = \left(\int_0^{T_{\max}} v_x dt \right) \sin\left(\frac{\pi}{6}\right) + \left(\int_0^{T_{\max}} v_y dt \right) \cos\left(\frac{\pi}{6}\right), \tag{15}$$

where u_{res} is the magnitude of the resultant displacement normal to the slant edge of the receiving wedge, v_x and v_y, respectively, are the velocity components in x and y directions, $T_{\max}$ is the maximum time or total time of the simulation, and $\frac{\pi}{6}$ rad is the wedge angle. Figs. 8(b) and (d), respectively, show displacements as functions of time measured at points on the receiving wedges of the standard clamp-on device and the PnC-embedded clamp-on device. These responses are calculated for $150\,\mu s$ with a time step of 66.67 ns. The shaded regions in these figures represent the time interval when the required signal reaches the receiver. As apparent in the figures, the maximum amplitude in the PnC-embedded system is four times lower than that of the standard system. This is
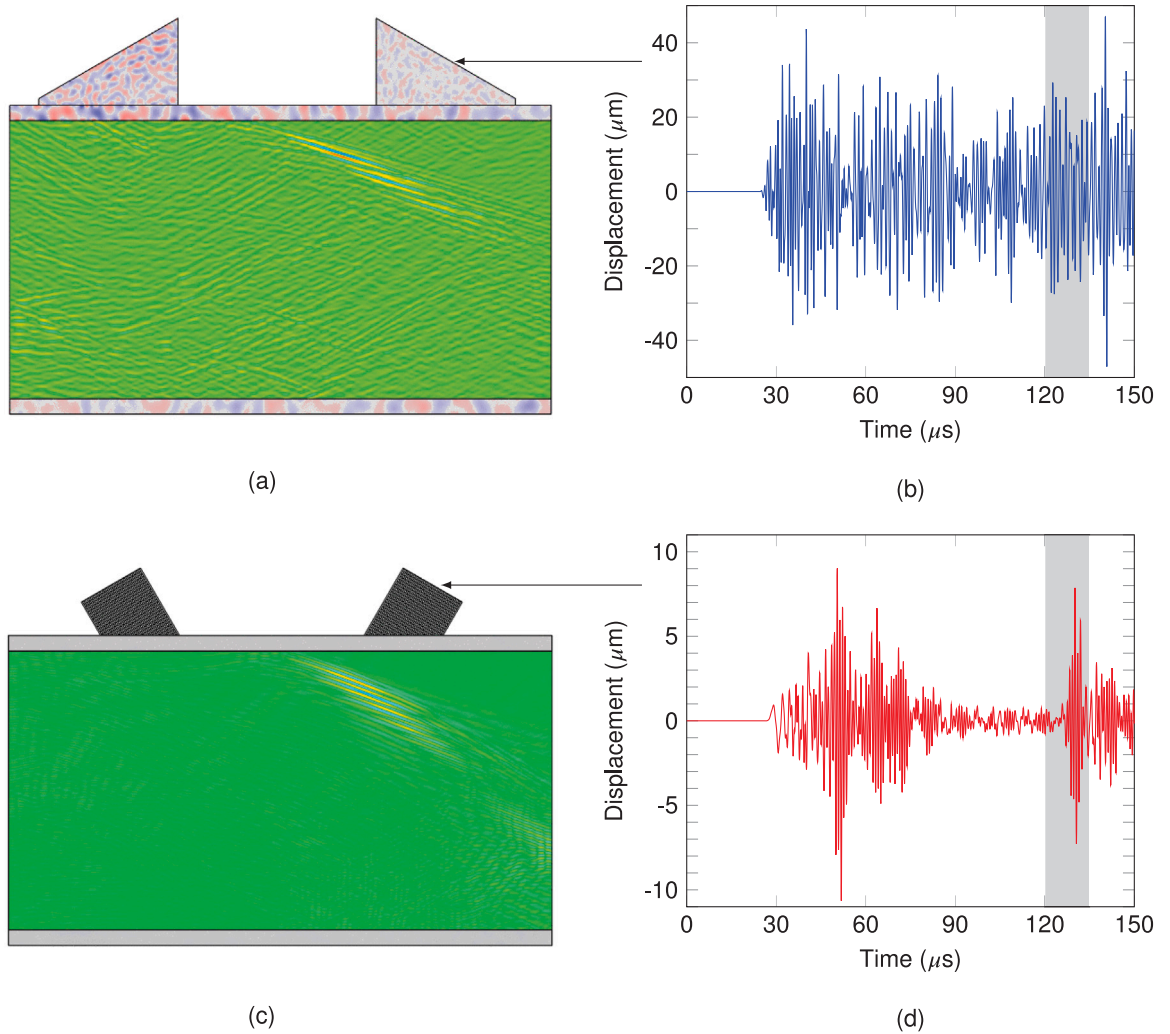
Fig. 8. Comparison of pressure and displacement responses of a clamp-on system with a standard wedge (top) and directional BG PnC embedded wedge (bottom). (a) and (c) are snapshots of the pressure profile of the standard clamp-on system and the clamp-on system with PnC-embedded wedges, respectively, for the time instance when the signal from the fluid is about to impinge the pipe wall ($t = 120\,\mu s$). (b) and (d) are the corresponding displacements (in μm) as functions of time (in μs) at the receiving wedges at the locations marked with arrows. Shaded regions in (b) and (d) show the time range corresponding to the arrival time of the signal from the fluid.

because the peak displacement in the standard system is dominated by the solid signals which were mostly filtered out by the PnC wedge. Since the PnC units do not cause any resistance to the principal wave path (as evident from the band structure in Fig. 6 and transmissibility relation in Fig. 7), the energy loss of the fluid signal will be minimal. Moreover, the standard clamp-on system has displacement peaks throughout the simulation time, making it difficult to identify the fluid's required signal. On the contrary, we can clearly distinguish the required signal from the displacement plot of the PnC-embedded clamp-on system.

3.3.2. Comparison of signal-to-noise ratio

To further inspect the quality of the receiving signal, we use signal-to-noise ratio (SNR) [58], which for a time series is obtained by

$$\text{SNR(dB)} = 10\log_{10}\left(\frac{P_s}{P_N}\right), \tag{16}$$

where P_s and P_N, respectively, are the power levels of the signal and noise pulses. We use the square of the displacement signal at the receiving wedge (refer to Figs. 8(b) and (d)) to calculate P_s and P_N, where we select the peak corresponding to the fluid pulse's arrival time for signal and an adjacent peak for noise. For the system with standard wedges, we obtain the SNR to be 0.83 dB, whereas, for the system with PnC embedded wedges, the SNR turned out to be 20.4 dB, which is 19.6 dB higher than that of the standard wedge system. Thus, the quality of the receiving signal has drastically improved due to the addition of PnC structures.
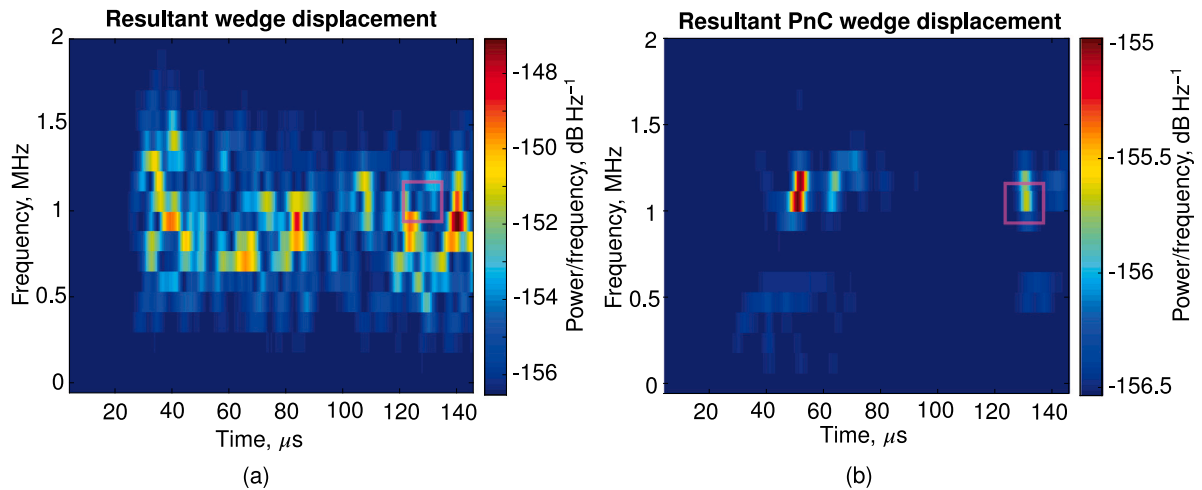
Fig. 9. Spectrograms for the standard wedge (a) and the PnC-embedded wedge (b) corresponding to the displacement response from Fig. 8. The abscissa is the total time in μs, the ordinate is the frequency in MHz, and the color code represents the power distribution of the signal per frequency shown using dB/Hz. Purple squares in both plots display the region of interest in time and frequency domains, where we can see the clamp-on system with PnC-embedded wedge is less noisy. (For interpretation of the references to color in this figure legend, the reader is referred to the web version of this article.)

3.3.3. Spectrogram comparison

To further check the influence of PnCs on the frequency spectrum of the output signal, we use a spectrogram, which visually represents the signal in time and frequency domains [59]. In this way, we can observe the signal strength at different frequencies and its variation over time. The time series is bundled into different overlapping time buckets, and their frequency responses are obtained via a short-time Fourier transform [59].

Figs. 9(a) and 9(b), respectively, show spectrogram representations of the displacement time series from Figs. 8(b) and (d). Here, the abscissa represents time (μs), the ordinate describes frequency (MHz), and the color spectrum shows the signal strength in terms of power per frequency (dB/Hz). The regions marked by purple squares in both plots show the region of interest in both time and frequency domains, i.e., f close to 1 MHz and t from 120 μs to 130 μs. Similarly to the displacement plots (Figs. 8(b) and (d)), the signal strength is lower for the clamp-on system with PnCs as compared to the standard one. However, from Fig. 9 it is apparent that the displacement signal from the standard wedge close to the required time (time of arrival of the signal through the fluid) is noisy in both time and frequency. In other words, the signal has many higher- and lower-order frequency components close to 1 MHz that span nearly the required time, making it difficult to detect the signal. Conversely, in the case of the clamp-on system with PnCs, the displacement signal close to the required time is relatively clean in both time and frequency domains, making it easier to identify the signal. Additionally, while using the clamp-on system with PnC-embedded wedges for flow measurement, we may be able to avoid using other filters, such as a frequency filter, since the receiving transducer already has less noise.

4. Summary and conclusions

To alleviate crosstalk in clamp-on ultrasonic flowmeters, we proposed a novel wedge design comprised of phononic crystals possessing directional band gaps. Using band structure and transmissibility analyses, we performed the forward design of the PnC structures to match the required frequency and wave vector ranges. The performance of the clamp-on ultrasonic flowmeter with PnC-embedded wedges was compared against a standard clamp-on system using wave propagation analysis, and we observed an enormous reduction in noise levels in the pipe wall. We also showed that by using the new wedges, we could obtain an improvement of 19.6 dB in signal-to-noise ratio as compared to a standard wedge. We conclude that:

- To remove acoustic/elastic noise from the clamp-on system, it is beneficial to understand the type (P or S wave) and behavior (ideal or non-ideal) of the signal, along with the frequency. This provides us additional information to target a particular signal type separately and eliminate them effectively;
- When there are multiple interfaces in the wave propagation system, waveguiding can effectively reduce the noise generated due to multiple reflections at various interfaces. By limiting these interactions through waveguiding in specific directions, we can prevent noises from entering the system, which can tamper with measurements;
- Current wave filtration methods that rely on time by identifying the signal in time and slicing the required time window and frequency; they remove low and high-frequency signals with band-pass or other types of filters. Therefore, they could be less effective when the receiving signal and noise are of similar frequencies and arrival times. Thus, we proposed a new kind of wave filtration method based on directionality. We can filter the noise close to the required signal by using directional waveguides that allow only the required signal to pass through, although the noise has the same frequency and time of arrival;

Our investigation shows that directional band gap phononic crystals can considerably improve clamp-on ultrasonic flowmeters' performance by mitigating the noise signals traveling through the solid and fluid regions. The directional filter concept we developed using the directional BG PnC structures possesses immense potential not just in clamp-on ultrasonic devices but also in other similar fields such as non-destructive testing and acoustic imaging. This is because using directional PnCs the initial signal shape is retained while interferences from unwanted directions are removed. Additionally, these PnC structures can also be designed to induce polarization thereby only exciting particular wave modes (e.g., P or S waves) that can aid in determining specific material properties (shear modulus or Poisson's ratio) accurately, which is otherwise cumbersome. Additionally, this method could be used with the existing filtration (time and frequency) techniques to augment the accuracy of sensing devices further. Noteworthy, introducing directional band gap phononic crystals reduces the overall signal strength, which in the present case was almost entirely from the noise (solid signal). The future step is to realize such a directional band gap phononic wedge and validate experimentally in a clamp-on setting.

CRediT authorship contribution statement

Sabiju Valiya Valappil: Writing – original draft. **Alejandro M. Aragón:** Writing – review & editing, Supervision. **Johannes F.L. Goosen:** Writing – review & editing, Supervision.

Declaration of competing interest

The authors declare the following financial interests/personal relationships which may be considered as potential competing interests: J.F.L. Goosen reports financial support was provided by topconsortium voor kennis en innovatie (TKI) and KROHNE. If there are other authors, they declare that they have no known competing financial interests or personal relationships that could have appeared to influence the work reported in this paper.

Acknowledgment

Appendix A. Supplementary data

Supplementary material related to this article can be found online at https://doi.org/10.1016/j.ymssp.2024.112173.

Data availability

The raw data supporting this study's findings are available from the corresponding author on request.

References

[1] Global Flow Meter Market Size Report, 2021–2028, Grand View Research, 2020.

[2] Richard Smith, Douglas R. Sparks, Diane Riley, Nader Najafi, A MEMS-based coriolis mass flow sensor for industrial applications, IEEE Trans. Ind. Electron. 56 (4) (2009) 1066–1071.

[3] Mahmoud Meribout, Abdelwahid Azzi, Nabil Ghendour, Nabil Kharoua, Lyes Khezzar, Esra AlHosani, Multiphase flow meters targeting oil & gas industries, Measurement 165 (2020) 108111.

[4] M. Kupnik, A. Schroder, P. O'Leary, E. Benes, M. Groschl, Adaptive pulse repetition frequency technique for an ultrasonic transit-time gas flowmeter for hot pulsating gases, IEEE Sens. J. 6 (4) (2006) 906–915.

[5] Yong Chen, Yiyong Huang, Xiaoqian Chen, Acoustic propagation in viscous fluid with uniform flow and a novel design methodology for ultrasonic flow meter, Ultrasonics 53 (2) (2013) 595–606.

[6] H.-H. Eckstein, M. Eichbaum, K. Klemm, A. Doerfler, P. Ringleb, T. Bruckner, J.-R. Allenberg, Improvement of carotid blood flow after carotid endarterectomy—Evaluation using intraoperative ultrasound flow measurement, Eur. J. Vasc. Endovascular Surg. 25 (2) (2003) 168–174.

[7] R.C. Baker, Flow measurement handbook, in: Flow Measurement Handbook: Industrial Designs, Operating Principles, Performance, and Applications, Cambridge University Press, 2016.

[8] M.L Sanderson, H. Yeung, Guidelines for the use of ultrasonic non-invasive metering techniques, Flow Meas. Instrum. 13 (4) (2002) 125–142.

[9] Furio Cascetta, Application of a portable clamp-on ultrasonic flowmeter in the water industry, Flow Meas. Instrum. 5 (3) (1994) 191–194.

[10] Americo Zuzunaga, Bob Maron, A Survey of Non-Invasive and Semiinvasive Flow Meters for Mining Applications: Understanding and Selecting the Right Technology for the Application, CiDRA Minerals Processing, Wallingford, USA, 2013.

[11] I.A. Viktrov, Rayleigh and Lamb Waves: Physical Theory and Applications, Plenumn, 1967 (Chapter II).

[12] Kenichi Tezuka, Michitsugu Mori, Sanehiro Wada, Masanori Aritomi, Hiroshige Kikura, Yukihiro Sakai, Analysis of ultrasound propagation in high-temperature nuclear reactor feedwater to investigate a clamp-on ultrasonic pulse Doppler flowmeter, J. Nucl. Sci. Technol. 45 (8) (2008) 752–762.

[13] Chuangnan Wang, Tim Stevenson, Will Vickers, Tim P. Comyn, Wedge design for high-temperature ultrasonic flow rate measurement, Sensors Actuators A 298 (2019) 111585.

[14] Simon Haykin, K.J. Ray Liu, Handbook on Array Processing and Sensor Networks, John Wiley & Sons, 2010.

[15] Jack Massaad, Paul L.M.J. van Neer, Douwe M. van Willigen, Michiel A.P. Pertijs, Nicolaas de Jong, Martin D. Verweij, Suppression of lamb wave excitation via aperture control of a transducer array for ultrasonic clamp-on flow metering, J. Acoust. Soc. Am. 147 (4) (2020) 2670–2681.

[16] Jack Massaad, Paul L.M.J. Van Neer, Douwe M. Van Willigen, Emile C. Noothout, Nicolaas de Jong, Michiel A.P. Pertijs, Martin D. Verweij, Design and proof-of-concept of a matrix transducer array for clamp-on ultrasonic flow measurements, IEEE Trans. Ultrason. Ferroelectr. Freq. Control 69 (8) (2022) 2555–2568.

[17] Jack Massaad, Douwe van Willigen, Paul van Neer, Nicolaas de Jong, Michiel Pertijs, Martin Verweij, Acoustic design of a transducer array for ultrasonic clamp-on flow metering, in: 2019 IEEE International Ultrasonics Symposium, IUS, 2019, pp. 1133–1136.

[18] A. Bybi, S. Grondel, J. Assaad, A.-C. Hladky-Hennion, C. Granger, M. Rguiti, Reducing crosstalk in array structures by controlling the excitation voltage of individual elements: A feasibility study, Ultrasonics 53 (6) (2013) 1135–1140.

[19] M.S. Kushwaha, P. Halevi, L. Dobrzynski, B. Djafari-Rouhani, Acoustic band structure of periodic elastic composites, Phys. Rev. Lett. 71 (1993) 2022–2025.

[20] M.S. Kushwaha, P. Halevi, G. Martínez, L. Dobrzynski, B. Djafari-Rouhani, Theory of acoustic band structure of periodic elastic composites, Phys. Rev. B 49 (1994) 2313–2322.

[21] W.L. Bragg, The diffraction of short electromagnetic waves by a crystal, Scientia 23 (45) (1929) 153.

[22] Matthew Reynolds, Stephen Daley, An active viscoelastic metamaterial for isolation applications, Smart Mater. Struct. 23 (4) (2014) 045030.

[23] J. Xu, J. Tang, Tunable prism based on piezoelectric metamaterial for acoustic beam steering, Appl. Phys. Lett. 110 (18) (2017) 181902.

[24] Shu Zhang, Chunguang Xia, Nicholas Fang, Broadband acoustic cloak for ultrasound waves, Phys. Rev. Lett. 106 (2) (2011) 024301.

[25] Kyung Ho Sun, Jae Eun Kim, Jedo Kim, Kyungjun Song, Sound energy harvesting using a doubly coiled-up acoustic metamaterial cavity, Smart Mater. Struct. 26 (7) (2017) 075011.

[26] Choon Mahn Park, Jong Jin Park, Seung Hwan Lee, Yong Mun Seo, Chul Koo Kim, Sam H. Lee, Amplification of acoustic evanescent waves using metamaterial slabs, Phys. Rev. Lett. 107 (2011) 194301.

[27] Gang Yong Song, Bei Huang, Hui Yuan Dong, Qiang Cheng, Tie Jun Cui, Broadband focusing acoustic lens based on fractal metamaterials, Sci. Rep. 6 (2016) 35929.

[28] Yafeng Chen, Fei Meng, Guangyong Sun, Guangyao Li, Xiaodong Huang, Topological design of phononic crystals for unidirectional acoustic transmission, J. Sound Vib. 410 (2017) 103–123.

[29] Xiaopeng Zhang, Jian Xing, Pai Liu, Yangjun Luo, Zhan Kang, Realization of full and directional band gap design by non-gradient topology optimization in acoustic metamaterials, Extreme Mech. Lett. 42 (2021) 101126.

[30] Sabiju Valiya Valappil, Johannes F.L. Goosen, Alejandro M. Aragón, Phononic crystals for suppressing crosstalk in ultrasonic flowmeters, IEEE Trans. Instrum. Meas. 72 (2023) 1–11.

[31] Sabiju Valiya Valappil, Johannes F.L. Goosen, Alejandro M. Aragón, Multi-objective design of 3D phononic crystal waveguide by design space trimming, Mater. Des. 237 (2024) 112594.

[32] Ralf Lucklum, Nikolay Mukhin, Enhanced sensitivity of resonant liquid sensors by phononic crystals, J. Appl. Phys. 130 (2) (2021) 024508.

[33] Nikolay Mukhin, Mykhailo Kutia, Aleksandr Oseev, Ulrike Steinmann, Stefan Palis, Ralf Lucklum, Narrow band solid-liquid composite arrangements: Alternative solutions for phononic crystal-based liquid sensors, Sensors 19 (17) (2019).

[34] A. Oseev, M. Zubtsov, R. Lucklum, Octane number determination of gasoline with a phononic crystal sensor, Procedia Eng. 47 (2012) 1382–1385, 26th European Conference on Solid-State Transducers, EUROSENSOR 2012.

[35] A. Oseev, M. Zubtsov, R. Lucklum, Gasoline properties determination with phononic crystal cavity sensor, Sensors Actuators B 189 (2013) 208–212, Selected Papers from the 26th European Conference on Solid-State Transducers.

[36] M. Miniaci, A.S. Gliozzi, B. Morvan, A. Krushynska, F. Bosia, M. Scalerandi, N.M. Pugno, Proof of concept for an ultrasensitive technique to detect and localize sources of elastic nonlinearity using phononic crystals, Phys. Rev. Lett. 118 (2017) 214301.

[37] Elizabeth J. Smith, Kathryn H. Matlack, Metal additively manufactured phononic materials as ultrasonic filters in nonlinear ultrasound measurements, J. Acoust. Soc. Am. 149 (6) (2021) 3739–3750.

[38] Geoffrey Roger Sherwood, Dimitrios Chronopoulos, Andrea Marini, Francesco Ciampa, 3D-printed phononic crystal waveguide transducers for nonlinear ultrasonic damage detection, NDT & E Int. 121 (2021) 102456.

[39] Menglong Liu, Zhihui Zeng, Hao Xu, Yaozhong Liao, Limin Zhou, Zhong Zhang, Zhongqing Su, Applications of a nanocomposite-inspired in-situ broadband ultrasonic sensor to acousto-ultrasonics-based passive and active structural health monitoring, Ultrasonics 78 (2017) 166–174.

[40] Minoo Kabir, Amir Mostavi, Didem Ozevin, Noise isolation with phononic crystals to enhance fatigue crack growth detection using acoustic emission, J. Civ. Struct. Health Monit. 8 (3) (2018) 529–542.

[41] Antonio S. Gliozzi, Marco Miniaci, Federico Bosia, Nicola M. Pugno, Marco Scalerandi, Metamaterials-based sensor to detect and locate nonlinear elastic sources, Appl. Phys. Lett. 107 (16) (2015) 161902.

[42] Francesco Ciampa, Akash Mankar, Andrea Marini, Phononic crystal waveguide transducers for nonlinear elastic wave sensing, Sci. Rep. 7 (1) (2017) 14712.

[43] Paweł Kudela, Maciej Radzienski, Marco Miniaci, Piotr Fiborek, Wiesław Ostachowicz, An ultrasensitive device with embedded phononic crystals for the detection and localisation of nonlinear guided waves, 2024.

[44] Fang Q. Hu, M.Y. Hussaini, Patrick Rasetarinera, An analysis of the discontinuous Galerkin method for wave propagation problems, J. Comput. Phys. 151 (2) (1999) 921–946.

[45] J.B. Rose, Preparation and properties of poly(arylene ether sulphones), Polymer 15 (7) (1974) 456–465.

[46] Daniel Royer, Eugene Dieulesaint, Elastic Waves in Solids I: Free and Guided Propagation, Springer Science & Business Media, 1999.

[47] Gang Bao, Yixian Gao, Peijun Li, Time-domain analysis of an acoustic–elastic interaction problem, Arch. Ration. Mech. Anal. 229 (2) (2018) 835–884.

[48] COMSOL, Acoustics module user's guide, COMSOL Multiphys. 6 (16) (2018) 354–370.

[49] J. Dellinger, J. Etgen, Wave-field separation in two-dimensional anisotropic media, Geophysics 55 (7) (1990) 914–919.

[50] Hejun Zhu, Elastic wavefield separation based on the Helmholtz decomposition, Geophysics 82 (2) (2017) S173–S183.

[51] Charles Kittel, Paul McEuen, Introduction to Solid State Physics, John Wiley & Sons, 2018.

[52] Karl F. Graff, Wave Motion in Elastic Solids, Courier Corporation, 2012.

[53] Felix Bloch, Quantum mechanics of electrons in crystal lattices, Z. Phys. 52 (1928) 555–600.

[54] István L. Vér, Leo L. Beranek, Noise and Vibration Control Engineering: Principles and Applications, John Wiley & Sons, 2005.

[55] Thomas J.R. Hughes, The Finite Element Method: Linear Static and Dynamic Finite Element Analysis, Courier Corporation, 2012.

[56] Sabiju Valiya Valappil, Alejandro M. Aragón, Hans Goosen, Phononic crystals' band gap manipulation via displacement modes, Solid State Commun. (2022) 115061.

[57] L. D'Alessandro, E. Belloni, R. Ardito, A. Corigliano, F. Braghin, Modeling and experimental verification of an ultra-wide bandgap in 3D phononic crystal, Appl. Phys. Lett. 109 (22) (2016) 221907.

[58] Don H. Johnson, Signal-to-noise ratio, Scholarpedia 1 (12) (2006) 2088.

[59] Wenkai Lu, Fangyu Li, Seismic spectral decomposition using deconvolutive short-time Fourier transform spectrogram, Geophysics 78 (2) (2013) V43–V51.